

Experimental verification of the frozen flow atmospheric turbulence assumption with use of astronomical adaptive optics telemetry

Lisa Poyneer,^{1,*} Marcos van Dam,^{2,3} and Jean-Pierre Véran⁴

¹Lawrence Livermore National Laboratory, 7000 East Avenue, Livermore, California 94550, USA

²W. M. Keck Observatory, 65-1120 Mamalahoa Highway, Kamuela, Hawaii 96743, USA

³Current address: Applied Research Associates New Zealand, Ltd. (ARANZ), St Elmo Courts, 47 Hereford St., Christchurch, New Zealand

⁴Herzberg Institute of Astrophysics, 5071 West Saanich Road, Victoria, British Columbia, Canada V9E2E7

*Corresponding author: poyneer1@llnl.gov

Received October 7, 2008; revised November 26, 2008; accepted December 1, 2008;
posted January 16, 2009 (Doc. ID 102440); published March 18, 2009

We use closed-loop deformable mirror telemetry from Altair and Keck adaptive optics (AO) to determine whether atmospheric turbulence follows the frozen flow hypothesis. Using telemetry from AO systems, our algorithms (based on the predictive Fourier control framework) detect frozen flow >94% of the time. Usually one to three layers are detected. Between 20% and 40% of the total controllable phase power is due to frozen flow. Velocity vector RMS variability is less than 0.5 m/s (per axis) on 10-s intervals, indicating that the atmosphere is stable enough for predictive control to measure and adapt to prevailing atmospheric conditions before they change. © 2009 Optical Society of America

OCIS codes: 010.1080, 101.1330, 010.7060.

1. PREDICTIVE CONTROL PROPOSALS AND KNOWLEDGE OF ATMOSPHERIC BEHAVIOR

In currently operating astronomical adaptive optics (AO) systems, there is a time delay between the wavefront sensor (WFS) measurements and the application of new commands to the deformable mirror (DM). In addition, the WFS and DM both have stare times, while the WFS integrates and the DM holds the commanded shape. The atmospheric phase aberration changes during the lag and stares, reducing the effectiveness of the phase correction on the DM. This evolution of phase with time leads to a type of residual error called the temporal error. Temporal error can be significant and is a limiting factor in future high-performance AO systems such as the Gemini Planet Imager (GPI) [1] and SPHERE [2].

Predictive control can improve AO performance by explicitly correcting for the temporal evolution of the phase. This deals primarily with the lag but can also deal with the stare times. Prediction is an active area of AO research, with at least four new proposals in the past few years: the “Strehl-optimal” approach of Gavel and Wiberg [3], the closed-loop Kalman filtering approach of Le Roux *et al.* [4], the data-driven \mathcal{H}_2 -optimal method of Hinnen *et al.* [5], and our own method of predictive Fourier control (PFC) [6]. These methods all have strong foundations in control systems and signal processing theory and provide a solid theoretical framework for prediction. PFC distinguishes itself from the alternatives both in being computationally efficient enough to be implemented in GPI with

commercial, off-the-shelf computer hardware and in having a simple and effective algorithm for identifying, characterizing, and adapting its prediction to match the behavior of the atmosphere.

All these predictive algorithms require a model for the temporal evolution of the atmosphere. If the statistical characterization of the atmosphere embodied by this model accurately reflects present atmospheric conditions, the prediction will improve performance. If the model is wrong, a predictor will not improve performance and may even make things worse. PFC and other proposals enumerated above assume that the atmosphere follows the frozen flow hypothesis.

Astronomical AO systems correct phase aberrations that are caused by refractive index variations in the atmosphere along the optical path. The frozen flow hypothesis involves two assumptions about the temporal evolution of the atmosphere. First, the refractive index variations are concentrated in distinct layers and stay spatially stable through time. Second, these layers are blown by the wind, leading to a translation of the phase aberration across the pupil.

Before implementing a frozen-flow-based algorithm in a real astronomical AO system, it is essential that we determine whether frozen flow layers of atmospheric turbulence exist and contribute significantly to the dynamic phase aberration. There are few quantitative studies on frozen flow, though it is widely assumed in both predictive control proposals and in general AO modeling and simulation (see, for example, the analysis of Guyon [7] or Brit-

ton's Arroyo simulation tool [8]). Gendron and Léna [9] used the ComeOnPlus AO system at the European Southern Observatory 3.6 m telescope and calculated the spatiotemporal cross correlation of the WFS measurements of the 7×7 AO system. They observed "several occurrences" (no exact number was specified) of frozen flow during a campaign with 120 nights of observations. Schöck and Spillar [10] also used a postprocessing cross-correlation technique on WFS measurements from the two Air Force Research Laboratory (AFRL) Starfire Optical Range AO systems. Both systems have approximately 10 cm subapertures: the smaller 1.5 m telescope AO system is 16×16 , and the larger 3.5 m telescope AO system is 35×35 . They concluded that accurate wavefront predictions can be made under the assumption of frozen flow but only on the time scales of 1–10 ms. Neither of these results provide persuasive justification for implementing a predictive control algorithm based on the frozen flow assumption.

To address the question of whether frozen flow is a good enough assumption that it can be used to improve AO performance, in particular when PFC is used, we have embarked on a campaign using telemetry from existing astronomical AO systems. In this paper we report results from observations with the Altair and Keck AO systems; these systems are described in Section 2. Though they do not operate with Fourier reconstruction, let alone the PFC algorithm, we can postprocess the telemetry as if they did. This allows us to use PFC's algorithms to identify frozen flow. This data analysis process is described in Section 3.

We present our results in Sections 4–6. We find that frozen flow exists and is strongly detected $>94\%$ of the time at Mauna Kea. For the spatial frequencies that Altair and Keck can measure and control, frozen flow normally causes between 20% and 40% of the total atmospheric power. For specific Fourier modes (spatial frequencies), this amount of power is higher and can be up to 70%. The velocity vectors of the layers of frozen flow are stable on time scales of seconds to minutes. Furthermore, we present an example where they are stable over 1 h. PFC, as proposed, will measure and adapt to the atmosphere every 10 s. The one-axis root mean square (RMS) variation of the layer velocity vectors in 0.5 m/s on 10-s intervals, which is low enough not to significantly degrade PFC performance, even for GPI.

2. ASTRONOMICAL ADAPTIVE OPTICS SYSTEMS USED

We use AO telemetry from closed-loop operation of Gemini North's Altair AO system [11] and the W. M. Keck Observatory's natural guide star (NGS) AO system [12]. Both of these large telescopes are located on the summit of Mauna Kea, on the island of Hawai'i. Both systems have Shack–Hartmann WFSs matched to square-grid actuator DMs, providing a fixed spatial sampling set by the subaperture size. Though both systems suffer from aliasing in the WFS [13], this does not limit our ability to detect frozen flow, as will be shown below. We begin with a discussion the key characteristics of these two AO systems.

A. Keck AO

Keck AO operates with 0.56 m subapertures across the segmented hexagonal primary mirror, which has a collecting area equivalent to a 10 m circular telescope. For our observations, the system was operated in closed loop at 1054 Hz, with all telemetry saved. 30,000-element-long streams of AO telemetry were extracted at a time to form measurements. This provides up to 28.5 s of uninterrupted telemetry. Several such streams can be extracted sequentially to provide a longer interval of measurement. Most of our Keck AO telemetry was saved during regular science observation. We have only a small number of nights of observations (July 16, July 30, October 18, October 27, all in 2007) but up to several minutes of data at different points in time on those nights. These temporally disparate observations can be compared with proper adjustment for pointing and rotation, as will be described later.

Keck AO reconstructs the wavefront using a Bayesian method that incorporates a model of the covariance of Kolmogorov turbulence and WFS noise levels [12]. The closed-loop control is done with an integral controller with fixed coefficients. Due to the shape of the segmented Keck primary and its rotation, not all of the 349 actuators are adjacent to illuminated subapertures. As a result, the outer ring of actuators is discarded from the data analysis, resulting in an effective 20×20 AO system.

B. Altair

Altair has 12×12 subapertures across the 7.9 m pupil, resulting in 66 cm subapertures. All of our Altair observations were done during the initial tuning of the Gemini primary mirror, before regular science operation. In this M1-tuning operation, the AO system is locked on a bright star and the static aberrations that it senses are offloaded to the active primary mirror to perfect its shape. For these measurements, Altair was operated at 1000 Hz, with 61,440-element circular buffers saved at a time. This provides 61.4 s of uninterrupted observation of the atmosphere. Our Altair measurements are all single 1 min intervals over 117 different nights from April 2007 to April 2008.

Altair uses a modified Zernike modal basis for wavefront reconstruction. For these experiments modal gain optimization was used, but the bright-star targets made the gains all equal the maximum possible gain. The temporal control was done with an integral controller with this maximum gain.

3. TEMPORAL POWER SPECTRAL DENSITY ANALYSIS OF FOURIER MODES FROM TELEMETRY

Though neither AO system uses Fourier reconstruction, we can analyze the data as if they did. This analysis process converts the closed-loop telemetry of DM commands into estimates of the open-loop temporal power spectral densities (PSDs) of the Fourier modes of the atmosphere. This process, detailed step by step below, involves several key steps, including conversion from the spatial domain

to the Fourier domain, estimation of temporal PSDs, and adjustments for DM response (influence function) and the AO control loop behavior.

A. Fourier Reconstruction Concepts

Fourier transform wavefront reconstruction (FTR) [14,15] is a computationally efficient filtering method. It uses as its basis set the Fourier modes, which are the controllable spatial frequencies of the wavefront. For predictive control, we use complex-valued Fourier modes [6] instead of real-valued sine and cosine pairs. For a given pupil size D and subaperture size d , there are D/d subapertures across the pupil. The phase is reconstructed on an $N \times N$ grid. N is usually a few larger than D/d and is chosen for a computationally efficient discrete Fourier transform (DFT), e.g., FFTW [16]. The Fourier modes, when calculated with the DFT, are indexed by frequency variables k and l , take the values $-N/2, -(N/2-1), \dots, -1, 0, 1, \dots, (N/2-2), (N/2-1)$. This gives each Fourier mode the frequency components, in units of m^{-1} , $f_x = k/(Nd)$, and $f_y = l/(Nd)$.

B. Conversion to Fourier Modes

The processing begins by mapping the telemetry vector of DM commands into a square grid, which produces at each time step a two-dimensional image of the pupil. This is padded into an appropriately sized grid as if for FTR. For Altair, $N=16$; for Keck AO, $N=26$.

Any uncontrolled data points, such as those from slaved or extrapolated actuators, are discarded and set to zero. Based on provided system information with the telemetry, the data units are converted to nanometers of error. If it has not already been done, piston, tip, and tilt are removed from the signal. Finally, the Fourier modal coefficients are calculated with a DFT, using a normalization constant to preserve total power.

The DFT converts from the spatial domain to the frequency domain. This applies for all spatial signals in the control loop, including DM commands, residual phase, and WFS slopes. Because Fourier modes are eigenfunctions of linear, shift-variant systems, converting between the different types of signals (e.g., DM to phase, WFS to phase) simply involves filtering by transfer functions. Given a spatial signal $d[m,n]$ and the aperture $a[m,n]$, the modal coefficients are

$$D[k,l] = \left(\frac{1}{\sum_{m=0}^{N-1} \sum_{n=0}^{N-1} a[m,n]} \right)^{1/2} \sum_{m=0}^{N-1} \sum_{n=0}^{N-1} d[m,n] a[m,n] \times \exp(-j2\pi[mk + nl]/N). \quad (1)$$

These steps produce a properly normalized data cube of Fourier modal coefficients of the DM commands for all time steps in the observation. At any time step, the total power of the Fourier modes (just the sum of their magnitudes-squared) is equal to the mean squared error of the commands on the DM in the pupil.

C. Estimating Open-Loop Temporal Power Spectral Densities

The second major stage of the telemetry analysis is evaluating the temporal PSDs of the Fourier modes and cor-

rectly compensating for the effects of the control loop and the DM. Each temporal PSD estimate is done on segments of length S . The system frame rate f_s sets the maximum estimated temporal frequency of $f_s/2$. The length of the segment S sets the sampling in temporal frequency at f_s/S and hence the minimum frequency greater than zero which is estimated. For both Altair and Keck AO, $S=2048$, which is approximately 2 s. Many half-overlapping segments of length S samples are used to estimate the temporal PSD. Note that because the Fourier modes and their modal coefficients are complex valued, the temporal PSD estimate must be calculated on both the positive and negative temporal frequency ranges.

Given the noise levels in the data, we have chosen 10 s as the minimum length of time over which a temporal PSD estimate can be calculated. For this length we have nine half-overlapped intervals to calculate the periodogram from. We can also evaluate the data over longer intervals (such as the maximum 61.4 s of Altair and the 28.5 s of Keck AO). However, since PFC must quickly measure and adapt to the atmosphere, we desired as short an interval as possible.

Once the interval length is set, the first step in PSD estimation is to remove the estimated mean value of the Fourier mode from the time series. This is a standard technique (see Oppenheim *et al.* [17]) that allows more accurate PSD estimation. This mean removal subtracts the estimated static error from the signal over the entire interval. Note that this is not the same as removing the average value of the data from each sub interval of length S , which would result in underestimation of low-frequency power. For each Fourier mode, the temporal PSD is then estimated using the averaged modified periodogram technique (again, see [17] for a thorough discussion). The Hanning window $h[t]$ is used on half-overlapped intervals for best signal-to-noise ratio (SNR). In particular, the estimated temporal PSD is

$$\hat{P}(\omega) = \frac{1}{N_{\text{intervals}}} \sum_{i=0}^{N_{\text{intervals}}-1} \hat{P}_i(\omega), \quad (2)$$

where

$$\hat{P}_i(\omega) = \frac{1}{S} \frac{1}{S-1} \left| \sum_{t=0}^{S-1} \Phi_i[k,l,t] h[t] \exp(-j\omega t) \right|^2, \quad (3)$$

and $\Phi_i[k,l,t]$ is the i th interval. The discrete-time frequency ω is converted to the continuous-time frequency f with the equation $\omega = 2\pi f/f_s$. The temporal PSD is normalized by the power in the window such that the sum of the temporal PSD equals the variance of that modal coefficient. At this point the sum of the entire data cube is the time-averaged MSE on the DM, excluding the static error component.

All of our telemetry represents commands sent to the DMs. The response (influence function) of the DM will modify these commands, resulting in a phase correction different from the commands. (Both Altair and Keck pre-compensate the DM commands to account for this to ensure the best phase compensation during operation.) To accurately estimate the phase conjugated by the DM, we

must account for the influence function. For Altair a numerical model was used; for Keck AO an analytic model was used. Generating an influence function with appropriate sampling and grid size allows conversion to a frequency response with just a DFT. For each mode, the temporal PSD is scaled by the magnitude squared of the transfer function for that mode. For a detailed discussion of this technique of influence function compensation in the Fourier domain, see Poyneer and Dillon [18].

Finally, the response of the control system must be compensated for. Our treatment is based on the standard continuous/discrete-time hybrid system model as illustrated in Fig. 1 (also see Madec's chapter in Roddier [19]). The goal is to estimate the continuous-time temporal PSD of the atmosphere (given by ϕ) free of influence of the controller.

The WFS transfer function is $H_{\text{wfs}}(s)=[1-\exp(-sT)]/(sT)$, where $T=1/f_s$. The DM has the same sample and hold $H_{\text{wfs}}(s)=H_{\text{dm}}(s)$. The computational delay is $H_{\text{delay}}(s)=\exp(-s\tau)$, where τ is the controller delay in seconds. The compute delay can be determined by from first principles by summing all the delays (e.g., CCD read-out time, centroid computation time, matrix multiplication of the reconstructor) or experimentally by looking at the response of the AO system to noise using a white light source [12]. For the Keck AO system, these two values agree.

The specific control law $C(z)$ depends on the AO system and is provided with the telemetry. An integral controller, for example, would have $C(z)=g/(1-z^{-1})$. For use with the discrete-time transfer function and discrete-time sampled PSDs, $z=\exp(-sT)$ and $s=j\omega/f_s$. We used the closed-loop DM commands $d[t]$; they have temporal PSD

$$\hat{P}_d(\omega) = \left| \frac{H_{\text{dm}}(s)H_{\text{delay}}C(z)}{1 + H_{\text{wfs}}(s)H_{\text{dm}}(s)H_{\text{delay}}(s)C(z)} \right|^2 \times [P_\phi(\omega)|H_{\text{wfs}}(s)|^2 + P_v(\omega)], \quad (4)$$

which means they are a joint estimate of the atmosphere $P_\phi(\omega)$, which is modified by the WFS response, and the WFS noise $P_v(\omega)$. The transfer function in front is divided out to obtain an open-loop estimate from the DM commands. (Note that in this case, the transfer function is equal to 1 for the lowest frequencies, so little change is made. This is logical, as the temporal PSD of the DM commands must be very similar to the temporal PSD of the

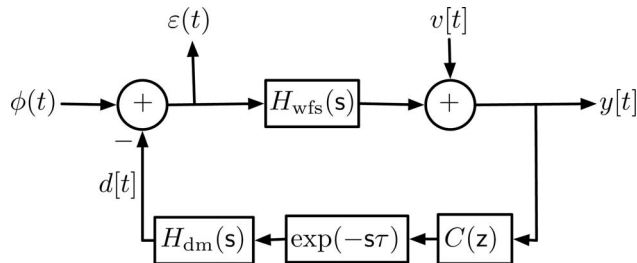


Fig. 1. Block diagram of hybrid continuous/discrete-time AO control loop for a single Fourier mode. The phase aberration $\phi(t)$ is corrected in closed loop in the presence of measurement noise $v[t]$. The WFS dynamics are represented by $H_{\text{wfs}}(s)$, the DM dynamics by $H_{\text{dm}}(s)$, and the controller delay by $\exp(-s\tau)$. The discrete-time control law is $C(z)$.

atmosphere, or else the AO loop would not provide good correction.) This estimate of $P_\phi(\omega)|H_{\text{wfs}}(s)|^2 + P_v(\omega)$ is then split into two parts. The noise level is estimated and fitted based on the high-frequency portion of the PSD, which is flat due to the noise floor. For the atmosphere's PSD $P_\phi(\omega)$, we need to search it only over a limited domain of -100 to 100 Hz. The temporal frequencies are limited by the maximum spatial frequency of the AO system and the wind velocity. The influence of $|H_{\text{wfs}}(s)|^2$ is negligible in this range, so we ignore it.

D. Predictive Fourier Control Concepts

PFC is a Kalman filtering algorithm that independently controls each Fourier mode under the assumption of frozen flow. A state space model is used to describe the behavior of the closed-loop AO system. The frozen flow atmosphere is also included in this state space model.

Under the assumption of frozen flow, each Fourier mode's temporal PSD has a compact and easily identifiable structure. A layer of frozen flow is assumed to follow a pure translation across the pupil with velocities v_x and v_y . As the layer translates across the pupil, the Fourier mode does as well. This results a pure oscillation of the Fourier modal coefficient's phase. The complex coefficient, in vector space, simply rotates around the origin.

The temporal frequency of this rotation is just the dot product of the frequency vector with the wave vector. In this way the wind velocity and the spatial frequency combine into a temporal frequency:

$$f_t = v_x f_x + v_y f_y = \frac{v_x k + v_y l}{Nd}. \quad (5)$$

Note that the temporal frequency f_t can be positive or negative. The sign tells the direction in which the modal-coefficient vector rotates. For PFC, we model each layer for each Fourier mode independently as a first-order autoregression, termed AR(1), which is characterized by the complex number α :

$$a[t] = \alpha a[t-1] + w[t]. \quad (6)$$

The process is driven by temporally white noise $w[t]$ with a specific variance σ_a^2 . The complex number α has magnitude just less than one. The phase of α sets how much the Fourier mode advances in a single time step. Adjusting for the AO frame rate f_s with its inverse the time step $T=1/f_s$, this phase is simply $2\pi T$ multiplied by Eq. (5).

For a layer modeled by α , the temporal PSD of that component is

$$P_\phi(\omega) = \frac{\sigma_a^2}{|1 - \alpha \exp(-j\omega)|^2}. \quad (7)$$

This PSD has a form close to the pure oscillation at f_t described above.

PFC measures the atmosphere's characteristics in closed loop by estimating $\hat{P}_\phi(\omega)$, in a manner very similar to the one described above. This PSD is searched for peaks that correspond to layers. The parameters (α, σ_a^2) are used to solve the algebraic Riccati equation (ARE) and determine the new predictive control law $C(z)$ for each mode. We use the model identification part of this process,

with slight modifications from the original proposal, to identify atmospheric parameters.

E. Peak Finding

Just as with PFC, we now have access to $\hat{P}_\phi(\omega)$ for each Fourier mode. This PSD is used to identify the atmospheric model parameters. When there are multiple layers of frozen flow, they simply add together in the PSD. To describe an arbitrary atmosphere of L layers, $L+1$ AR(1) processes are used. The first layer, $L=0$ is used to represent the slowly varying errors seen by the system. Since it is centered at 0 Hz, we refer to this term as “DC.” The layers are described by their autoregression parameters $\alpha_0, \alpha_1, \dots, \alpha_L$ and the variances of the driving noises $\sigma_{\alpha_0}^2, \sigma_{\alpha_1}^2, \dots, \sigma_{\alpha_L}^2$. The temporal PSD is simply

$$P_\phi(\omega) = \sum_{i=0}^L \frac{\sigma_{\alpha_i}^2}{|1 - \alpha_i \exp(-j\omega)|^2}, \quad (8)$$

because the layers are uncorrelated with each other. For our analysis, we assume that $\alpha_0=0.995$, to provide excellent low-temporal-frequency correction. For the layers, we use $|\alpha|=0.99$. For a few data sets, we have found it necessary to add another term, similar to the DC term, with a real-valued $\alpha=0.8$. This mild autoregression captures a phenomenon sometimes observed in the Altair data where there is substantial atmospheric power with a broad, flat profile extending beyond 100 Hz. This is usually not necessary, however.

Our model identification is just searching the PSD for the peak and identifying the α 's and σ_α^2 's. Since our original PFC proposal [14], we have refined the peak-finding algorithm. In addition to the optional $\alpha=0.8$ term mentioned above, we have refined the search-and-project steps. The modified algorithm is as follows:

1. Set range of PSD to search (usually -100 to 100 Hz).
2. Project $\hat{P}_\phi(\omega)$ onto the $\alpha_0=0.995$ PSD shape to estimate σ_0^2 .
3. Subtract DC-fitted PSD term from data; set to zero any data points with negative values.
4. (Not usually necessary) Project $\hat{P}_\phi(\omega)$ onto the $\alpha_1=0.8$ PSD shape, but only in the $|50|$ to $|100|$ Hz ranges. Use this to estimate the power σ_1^2 for this mild autoregression.
5. (Not usually necessary) Subtract this newly fitted PSD term from data; set to zero any data points with negative values.
6. Loop through the remaining steps until no more significant peaks are found or the maximum number of layer peaks have been found (in this case we use a maximum of four layers).

(a) Correlate the modified $\hat{P}_\phi(\omega)$ with a preset shape. This correlation can be done in the Fourier domain. The preset shape is the magnitude squared of the Fourier transform of the Hanning window. This sets the minimum feature size for detecting a temporal frequency component.

(b) Locate the frequency of the peak by using parabolic interpolation on the three frequency samples centered on the maximum value of the correlation function. If

the maximum value is greater than the significance threshold, proceed. Else, end the search. This step estimates the temporal frequency of the peak and is used to generate the complex-valued α_i .

- (c) Construct the PSD shape for this α_i .
- (d) Estimate the power level $\sigma_{\alpha_i}^2$ via projection of $\hat{P}_\phi(\omega)$ onto the PSD shape.
- (e) Subtract layer-fitted PSD term from data; set to zero any data points with negative values.

This algorithm produces a list of found peaks, each characterized by a temporal frequency and driving noise variance. In PFC, these parameters are used to solve the ARE and produce the new steady-state Kalman filter. Instead, we will use the peak parameters, as well as the PSDs themselves, to analyze the frozen flow content of the atmosphere.

4. TEMPORAL PSD STRUCTURE OF AO OBSERVATIONS

As summarized in Subsection 2.A of [6], under frozen flow the temporal PSD of either an actuator or a Zernike mode has a broad power-law structure (in particular, see Fig. 2 of that paper). In contrast, the structure of the temporal PSD of a Fourier mode exhibits peaks that have significant amounts of power and are asymmetric with respect to temporal frequency. The first step in our analysis of Altair and Keck AO telemetry is to inspect the temporal PSDs.

The hallmarks of frozen flow are clearly seen in the AO telemetry, as is shown in Fig. 2. The three panels of this figure show temporal PSDs from two different minute-long Altair observations and a half-minute Keck observation. (Longer intervals are used for highest SNR for display purposes.) In the top panel, a very strong peak at 3.6 Hz is visible. It has 72% of the total power for this Fourier mode. The $S=2048$ length is adequate to clearly distinguish this peak from the DC term at 0 Hz. Much smaller peaks are identified at -5.4 and -8.4 Hz.

The middle panel shows a case where a peak is much broader than expected. There is a clear peak at 7.7 Hz, and a broader peak region that the PSD-fit algorithm identifies as two peaks at -17.3 and -20.1 Hz. A much weaker peak is also identified at -8.2 Hz. These four peaks contain 45.7% of the total power for this Fourier mode.

The bottom panel shows a half-minute Keck AO observation. A peak at 6.2 Hz sticks out above the background strongly. Very minor peaks at -7.0 , -10.0 , and -14.4 Hz are identified by the peak-finding algorithm. These combined have 26.1% of the total power in the mode. Like this one, many Keck observations had clear vibrations at ± 30 Hz. These are believed to be caused by the primary mirror and are masked out of the data before application of our peak-finding algorithm.

All three of these example PSDs clearly have peaks away from 0 Hz that are asymmetric, as do most of the PSDs for all of the observations. These peaks, particularly the ones with higher temporal frequencies, will not be well corrected by a standard integral controller. An integral controller provides 100 times less correction (in

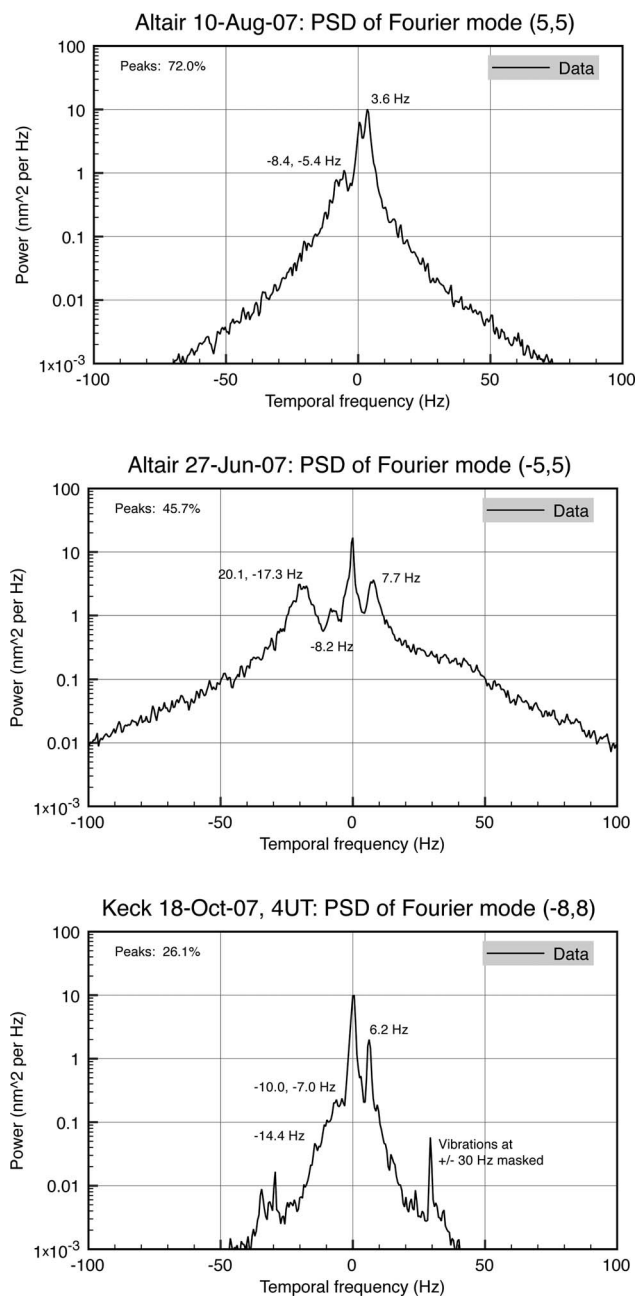


Fig. 2. Temporal PSDs of mid-frequency Fourier modes for (top), (middle) minute-long Altair observations and (bottom) a half-minute Keck AO observation. Note the clear presence of peaks not at 0 Hz and the lack of symmetry. The amount of total power in those peaks ranges from 26.1% to 72.0%.

terms of power) for a component at 10 Hz versus one at 1 Hz. PFC, in contrast, can selectively notch out a peak at an arbitrary frequency, providing improved residual error.

There are two significant differences in temporal PSD structure in the observational data, as compared to our AO simulations (for example, see Fig. 1 of [6]). First, the peak width is variable, and some peaks, such as in the middle panel of Fig. 2, have a width of several hertz. Second, the height of the peak relative to the background PSD shape is lower in the observational data. For example, in the bottom panel the peak at 6.2 Hz sticks out by about a factor of 10 from the background, but most of

the other peaks that were identified are less prominent. At this time the data provide us with no evidence to support a conclusion as to what physical process (e.g., boiling of the phase in each layer, variability of the layer velocity vector on subsecond time scales) causes these effects.

The peak-finding process determines not only the temporal frequency of the peaks but how much of the dynamic atmospheric power is in each peak, as well as the DC term. This amount of power can be analyzed for an individual Fourier mode or for all controllable spatial frequencies in the AO system.

Our 117 different nights of Altair data provide an adequate sample to study general behavior. First, we examine the power in the peaks, integrated over all controllable spatial frequencies. Figure 3, top panel, shows histograms of the percentage of atmospheric power found in the peaks for the controllable phase and for a specific midfrequency Fourier mode. For the controllable phase, the median amount of power in the layer peaks is 30%. The middle 95% of the cases range from having 20% to 56% of the total power.

Because of the $-11/3$ Kolmogorov power law of atmospheric power as a function of spatial frequency, this integral is dominated by the lowest Fourier modes, which have the least amount of power in the peaks. This is pri-

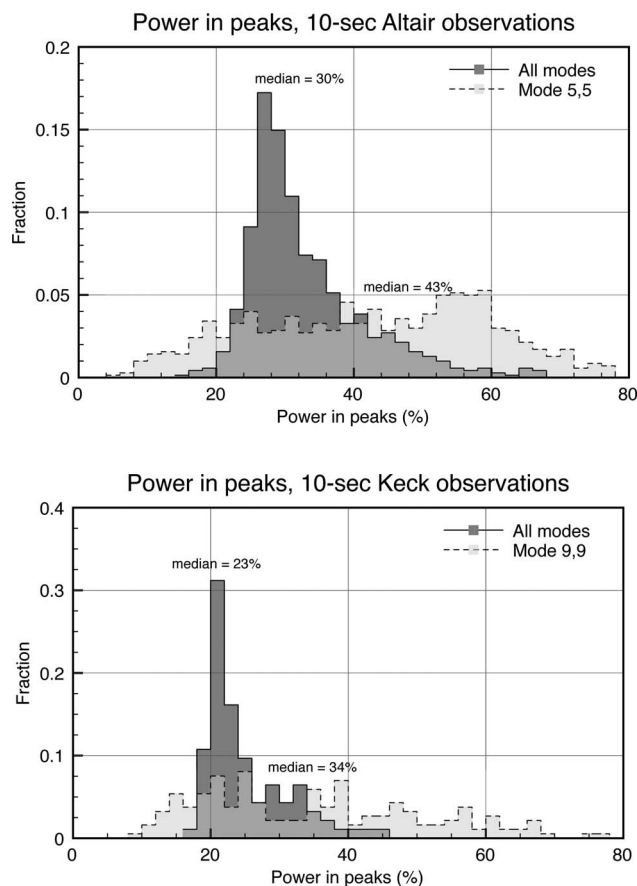


Fig. 3. Histograms of fraction of atmospheric power in the PSD peaks, for (top) all 10-s observations over 117 nights with Altair and (bottom) all 10-s Keck observations over five nights. In both cases, a moderate amount of total phase power is in the peaks, while for a specific mid-frequency Fourier mode much more power is in the peaks.

marily because the peaks caused by frozen flow have very low temporal frequencies in low-order Fourier modes. Hence they are hard to distinguish from the DC term. When we examine individual Fourier modes at higher spatial frequencies, they will have more power in the peaks, primarily because the peaks are clearly distinguishable from 0 Hz. For the Fourier mode $\langle 5,5 \rangle$, the median is 43% and the distribution is much broader and flatter. The middle 95% of the cases range from having 10% to 70% of the total power for that mode.

The Keck AO data represent a small, and probably non-representative, sample of Mauna Kea conditions. Nonetheless, the power amounts in the peaks are quite similar, as in shown in the bottom panel of the figure. In this case for all spatial frequencies, the median amount of power in the peaks is 23%, with the middle 95% of cases ranging from 20% to 40% of the total phase power. For a mid-spatial-frequency mode $\langle 9,9 \rangle$, the distribution is again quite broad. The mean power amount in the peaks is 34%, with the middle 95% of the cases spread from 12% to 66% of the power in that mode.

The percentages 20% to 40% of the total phase power may not seem like a lot. But almost all of the rest of the power is in the DC term, which is very well corrected by the integral controller. The 20% to 40% of power in the peaks is not well corrected. For an ExAO system such as GPI, where the subaperture spacing is three times smaller than Keck AO, we would expect this trend to continue, and the temporal frequencies of the peaks will be up to three times higher than at Keck. This means not only will more power be in frozen flow, it will be at a higher temporal frequency, making the performance improvement of PFC more significant.

5. IDENTIFYING LAYERS OF FROZEN FLOW

A. Quantifying Layer Velocities

Both Altair and Keck AO observational data clearly show the hallmark of frozen flow: peaks of power away from 0 Hz. The PFC algorithm, as proposed, will identify these peaks for each Fourier mode and then generate a predictive controller that will correct them. So in a sense, the actual source of the peak is irrelevant; the PFC algorithm will provide better temporal correction regardless of the cause. A good example of this is vibration, since this will appear as a \pm pair of peaks that PFC will correct. (The predictive Kalman filtering method has been successfully used to correct vibration, as was experimentally shown by Petit *et al.* [20])

However, we seek to verify that these peaks are actually caused by frozen flow. Starting from actual layers of frozen flow in the atmosphere, the AO system operates in closed loop and saves telemetry, and then the PFC algorithms convert the DM commands into a data cube of peaks found at specific temporal frequencies. The data cube for Altair observation 10-Feb-08, with each set of peaks shown, is the top row of Fig. 4. Here, we see the $\langle f_x, f_y \rangle$ domain of Fourier modes, and the color at each location represents the temporal frequency of the peak that was found.

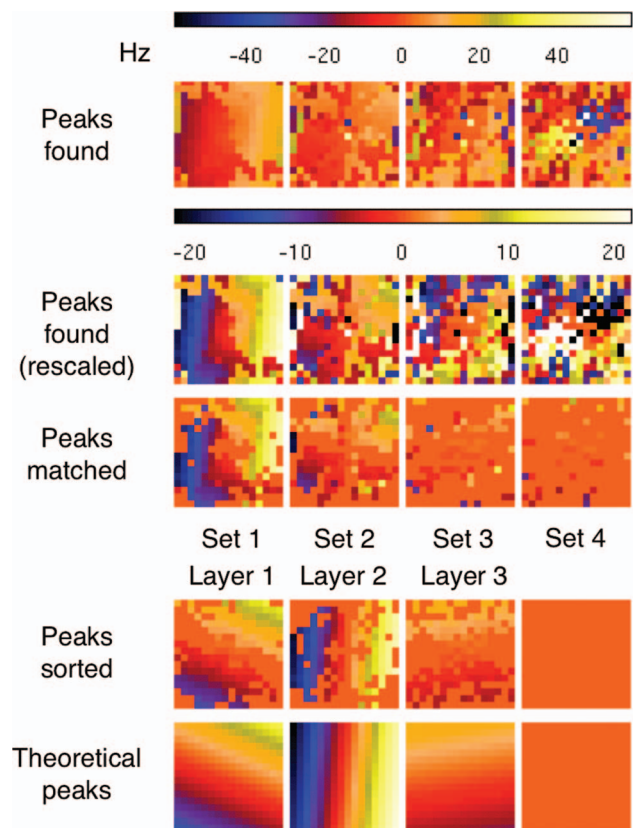


Fig. 4. Process of determining layers from peaks found. Color scales represent temporal frequency of the peak in hertz. (Any spatial frequency where no peak was found is illustrated as $f_t = 0$.) Across each row, there are four square panes, each of which shows the $\langle f_x, f_y \rangle$ Fourier modes for Altair. In the “Peaks found” row, the sets are sorted in the order in which the peaks were found for each mode. The yellow/blue areas in Set 4 are due to Layer 2 aliasing. In the “Peaks found (rescaled)” row, the color scale has been reduced. In “Peaks matched,” only the peaks that correspond to strongly found layers via the wind map are shown. Note how the aliases are excluded. In “Peaks sorted,” the peaks are moved from sets to layers. Set 1 contains peaks that belong to either Layer 1 or Layer 2. In “Theoretical peaks” the peak frequencies are given for a perfect detection of each layer. (These layers are the ones found in the wind map of Fig. 5.)

In order to verify that frozen flow caused these peaks in the PSDs, we need to reverse the process and go backward from the data cube to layers in the atmosphere. Our algorithm to do this is based upon the fundamental relationship between layers and peaks $f_t = v_x f_x + v_y f_y$. This means that when the Fourier modes are viewed on a f_x, f_y grid (as in Fig. 4), the temporal frequencies caused by that layer produce a plane, with piston ($f_x = f_y = 0$) always having a peak at 0 Hz. This is shown in the bottom row of the figure, where the “Theoretical peaks” are given for the eventual answer of our algorithm, which has found three layers.

In going from peaks found to layers, we need to match peaks to layers while ignoring spurious detections. Some peaks will match no layers, for a variety of reasons. These include noise in the temporal PSD estimate, the presence of vibrations, aliasing of uncontrollable spatial frequencies in the WFS, and potentially other unknown sources. In fact, the yellow and blue regions in “Set 4” of “Peaks found” are actually spatial aliases from Layer 2.

Our method for determining whether a layer of frozen flow exists is a straightforward but brute-force algorithm. We begin with a domain of possible velocity vectors that are evenly spaced on a square grid. For the Altair data, we searched from -60 to 60 m/s with resolution 0.5 m/s to generate a 241×241 grid. For Keck AO, we searched from -30 to 30 m/s with the same resolution. (The lesser diversity of Keck AO observations did not contain any very-high-velocity layers, hence the smaller search domain.)

For each velocity vector in this grid, we calculate the frequency plane $v_x f_x + v_y f_y$. Next, we search over each AO spatial frequency $\langle f_x, f_y \rangle$ where $|v_x f_x + v_y f_y| > 2$. We restrict the frequencies because the layer is not visible in the spatial frequencies that are orthogonal to the wind. For these, the peak is indistinguishable from the regular DC component of the atmosphere. For each Fourier mode that can detect that particular wind velocity, we search the set of found peaks for a peak that is close enough to the desired temporal frequency $f_t = v_x f_x + v_y f_y$. We define “close enough” as being within ± 0.75 Hz or 15% of the true value, whichever is less. This means for peak frequencies under 5 Hz, the found peak must be very close to the true value, which reduces false detections.

The likelihood of a layer existing is defined as the total number of modes that did find a “close enough” peak divided by the number of modes for which that wind velocity could potentially be detected. This metric is calculated for each velocity vector in the domain, producing a map of the likelihood of there being a layer. This algorithm is robust to false positives. Random peaks, vibrations, and aliases show up with likelihoods under 5%.

We refer to this likelihood mapping as a “wind map” for the observation. Figure 5 shows a wind map for the minute-long Altair measurement on 10-Feb-08. In this color wind map, there are three clearly identifiable concentrations of likelihood, indicating three layers.

In this case it is easy to “eyeball” the wind map and identify the three layers. To quantify and automate this process, and to be robust in situations where layers are

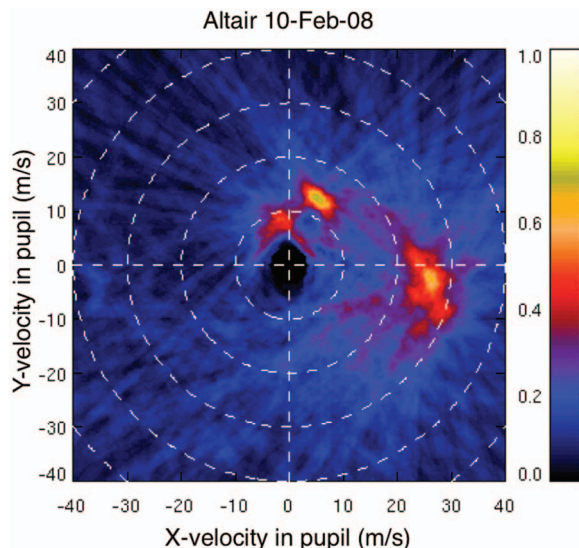


Fig. 5. Wind map showing likelihood (0 to 1) of a layer of frozen flow existing at a specific velocity vector, as observed by Altair.

closely located, we have applied the watershed algorithm. In this morphological algorithm, the image is segmented into regions that are associated with local minima. For our use, we apply the algorithm to the negative of the wind map, so that the local maxima are found. This allows us to determine, for example, whether a region of high likelihood in the wind map is from two neighboring layers (in which case there will be two watershed regions) or one. (See Gonzalez and Woods [21] for more details regarding this well-established algorithm). The result of the watershed algorithm is a segmentation of the image into layer regions, with a local maximum layer likelihood for each. We have set a threshold for a layer being “strongly detected” by the algorithm at 45% for the 10-s observations and 50% likelihood for longer observations. (This 10-s PSD estimate and hence peak temporal frequency estimates are more noisy. This necessitates a slightly lower threshold. This SNR issue is one that we plan to explore further.) In some cases a layer is clearly identifiable by eye but its likelihood is under the threshold. In those cases we do not classify that layer as strongly detected, though it may be readily apparent in the wind map.

Using the watershed algorithm, the most strongly detected layer in Fig. 5 has speed 13.3 m/s and angle 66° , with likelihood 73%. This layer is compact. The next layer is more diffuse; it has speed 26.4 m/s, angle -6° , and likelihood 65%. The weakest layer has speed 8.2 m/s and angle 99° , with likelihood 51%.

Now we return to Fig. 4 to illustrate the entire process. We begin with the data cube, shown in “Peaks found (rescaled).” Given the three layers that were found with the wind map, the row “Peaks matched” shows only those peaks that correspond to the layers. Note how most of the peaks in Set 3 and Set 4 do not match a strongly detected layer. The next row, “Peaks sorted,” shows the result of moving these matched peaks out of the sets and into layers. For example, some peaks in Set 1 correspond to Layer 1 and other peaks to Layer 2. The density of peaks filling the frequency map reflects the likelihood of that layer. Layer 1, as reported above, had a likelihood of 73%. In Layer 1 of “Peaks sorted,” 73% of the modes that could detect that layer have a peak present. In contrast, Layer 3, which had 51% likelihood, is more sparsely filled. Note how in all cases there is a region through piston where no peaks are ever found; this is because, as mentioned above, the layer temporal frequencies are too close to zero to be identified.

Our algorithms begin with the data cube of the temporal frequencies of the peaks found for all Fourier modes and convert this into a list of strongly detected layer velocity vectors. This enables us to study the characteristics of the frozen flow atmosphere.

B. Observed Atmospheric Characteristics

All the Altair and Keck AO observations were processed to detect layers of frozen flow turbulence, as described above. After this was done, at least one layer of frozen flow was found nearly all of the time. Figure 6 shows the number of strongly detected layers in each 10-s interval of observation. In the small, most likely nonrepresentative, sample of Keck AO data, we find at least one layer in 98% of the measurements; in the large 117-night Altair sample

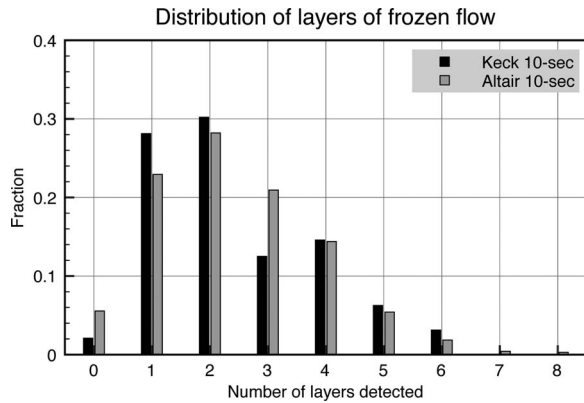


Fig. 6. Number of layers strongly detected in 10-s observations, for 117 different nights with Altair and five nights with Keck AO. At least one layer is strongly detected 94% of the time. For both AO systems, 1–3 layers are found >70% of the time, indicating that high-order prediction is not usually necessary.

we find at least one layer 94% of the time. In just over 70% of the observations, from one to three layers of frozen flow were strongly identified. This indicates that high-order predictive filters (e.g., six layers) are not usually necessary. For PFC, more layers means more computation to apply the predictive filter and more computation to solve for the new control.

We observe a large range of layer velocities. Figure 7 shows a histogram of all layers identified with at least 35% likelihood for the 117 Altair observations, on 10-s intervals. All layers with greater than 35% likelihood were used to get the largest possible sample, as faster wind speeds have lower likelihoods. (The justification for this is discussed in more detail below.)

Given the complexity of the atmospheric physics, as well as the uncertainties in the data regarding pointing, we do not attempt to formulate and verify the fit of a specific probabilistic model that explains layer wind speed variation. However, because an analytic form for the distribution of wind velocity may be necessary for system performance analysis, we provide a reasonable fit: a shifted log-normal distribution where $\sigma^2=1$, $\mu=2$,

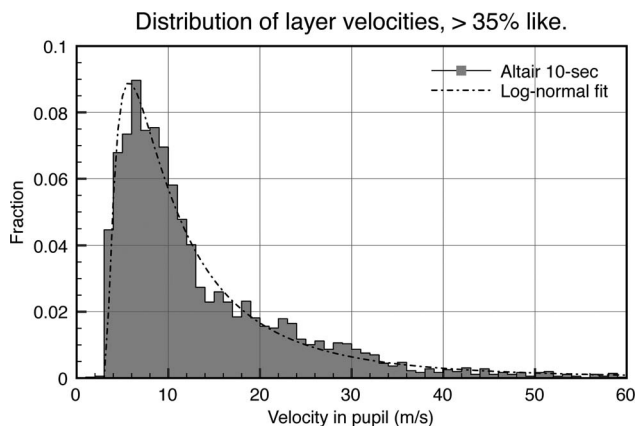


Fig. 7. Distribution of wind velocity for layers detected with likelihood >35%. Though half the layers have speed 10 m/s or less, there is a long tail to higher speeds. The Altair data are well fitted by a shifted log-normal distribution (see text for parameters).

$$p(v) = \frac{1}{(v-3)\sigma\sqrt{2\pi}} \exp\left(-\frac{[\ln(v-3)-\mu]^2}{2\sigma^2}\right) \quad \text{if } v > 3. \quad (9)$$

The layer-finding algorithm is insensitive to very slow layers. As such we cannot measure them, and the distribution is shifted to reflect this. This log-normal distribution is shown in the figure. This distribution is rejected by the Kolmogorov–Smirnov test at 85% confidence, but our data have measurement noise, and we cannot assume that they are uncorrelated samples from the same underlying distribution.

C. Assessing Algorithm Performance

In our characterization of the atmosphere’s frozen flow behavior, we are using measurements of it that are filtered through our algorithms. As such, we need to understand any inherent biases or noise levels in the process of running the AO system and applying the peak-finding and wind map algorithms to the telemetry data.

Since we cannot run a controlled experiment with either Altair or Keck AO, we instead use a simulation of an Altair-like AO system and a pure frozen flow atmosphere to place an upper bound on algorithm performance. For this simulation we use our standard Fourier optics AO simulation code (see Subsection 2.2 of Poyneer and Macintosh [22] for an in-depth discussion of the simulation) set up to match the Altair pupil, WFS geometry, and standard Shack–Hartmann WFS. For the input phase aberration, we use translation of large Kolmogorov phase screens, which are generated with the standard spectral factor method [23]. These screens, which are large enough that no repetition of phase occurs during the 10-s simulated run, are translated along precisely specified velocity vectors.

To test the quality of our algorithms in estimating both layer likelihoods and velocity vectors, we chose several three-layer wind profiles based on the Altair data. For each profile we assumed 14 cm r_0 distributed equally over the three layers and used a $I=9$ (bright) star for the AO run. For each case, we ran eight unique 10-s AO simulations with different atmospheric phase screen realizations. The telemetry from these runs were used to produce a set of eight different estimates of the wind profile.

With this, we find bounds on the accuracy of the algorithms detecting pure frozen flow in an idealized simulation. For the likelihood of the layer in the wind map, we find that it drops off monotonically, and in an approximately linear manner, with the wind speed of the layer. By 10 m/s wind speed, even pure frozen flow is identified with likelihood 90%. By 20 m/s the likelihood is 80%. This decrease in likelihood with wind speed is due to the fact that the estimate of the peak temporal frequency f_t becomes more noisy as the frequency increases. Since faster layers produce higher temporal frequencies, and our layer-matching algorithm uses a fixed $|f_t - \hat{f}_t| < C$ rule, faster layers inherently will have more peaks that do not match, entirely due to noise. As a result, faster layers will be less strongly detected, hence our decision above to include layers down to 35% likelihood to assess the velocity distribution out to 60 m/s.

D. Summary

To verify that the peaks found in each Fourier mode are actually caused by frozen flow, we have developed an algorithm that assesses the likelihood of a layer existing as a function of velocity vector. Using this, we verified that the peaks are due to layers. Out of 117 different nights of measurements spread out over one year, Altair AO sees frozen flow 94% of the time. The smaller set of Keck AO observations reveal frozen flow 98% of the time. Usually one to three layers are strongly identified. The speed of these layers can be approximated with a log-normal distribution. The median wind speed is 10 m/s, but a substantial tail exists out to 60 m/s in the Altair data.

6. TEMPORAL STABILITY OF LAYER VELOCITIES

In the previous sections we have shown how the frozen flow model is a good one for characterizing the atmosphere and that a substantial amount of total atmospheric phase power is due to frozen flow. Furthermore, we have shown that frozen flow is nearly always detected at Mauna Kea. This means a predictive control algorithm like PFC has the potential to provide improved performance in most observing conditions.

But besides having an appropriate model, the prediction algorithm must be able to quickly and accurately estimate the parameters that characterize the atmosphere (i.e., layer velocities and strengths). If the atmosphere changes structure too rapidly, this measure-and-adapt process will not be effective.

Our observations provide us with several ways to study layer variability. First, with the Altair data, we assess the variability of layer velocities on six consecutive 10-s intervals. The 117 nights of data provide us with an estimate of the inherent variability of a layer's velocity vector on short time scales. Second, with the Keck data, we track a specific case of atmospheric turbulence through time and show that layer velocity vectors can remain remarkably stable over a 1 h interval.

We finish with a direct measurement of the variability of the PFC controllers themselves, based on tracking the temporal frequencies of the peaks of in the Fourier mode PSDs. This variability is quite low and should not prevent effective prediction.

A. Altair Analysis

To analyze the Altair measurements, we use a simple statistical model to study the variation over the 1-min measurements. We first assume that the layer velocity is stationary over the 1-min observation; this means its average value and inherent variation do not change. We then track the layer velocity measurements through the six 10-s intervals and calculate the sample variance of the 10-s layer velocities. We calculate the unbiased sample variance s_N^2 , using the form that is divided by $N-1$, where N is the number of measurements. (This is as opposed to the biased sample variance that is divided by N .) If the underlying layer variability is relatively uniform across nights, the sample variances from all the layers on all the nights will have the distribution of a scaled chi-squared random variable with $N-1$ degrees of freedom

[24]. To estimate the inherent layer variance, we find the best chi-squared fit and estimate the layer variance σ^2 using the relationship that $(N-1)s_N^2/\sigma^2$ is distributed as $\chi^2(N-1)$. This distribution of layer sample variances is shown in Fig. 8, along with the best-fit chi-squared distribution. Using the strongly detected Altair layers, we estimate that the inherent RMS layer variability σ is between 0.38 and 0.50 m/s per axis.

Using the same simulations as mentioned above, we find bounds on the noise level for the algorithms detecting pure frozen flow in an idealized simulation. For the noise on the estimate of the precise layer velocity vector, we find that the one-axis RMS noise increases monotonically, and in an approximately linear fashion, with wind speed. For layers under 10 m/s, the RMS one-axis noise is under 0.05 m/s, a negligible value. For 20 m/s winds in our simulation, the one-axis RMS noise is 0.1 m/s. When compared to the histogram of estimated layer variabilities for the Altair measurements (Fig. 8), this indicates that the algorithm's inherent noise is not a significant factor. We therefore conclude that the above analysis of wind vector variability through time reflects actual variation in the atmosphere and not noise in the algorithm.

B. Keck Analysis

All the Altair observations are single 1-min intervals, each on a different night. Most of the Keck observations were taken sequentially on a few different nights. This allows us to track the atmosphere over several minutes and even, in one case, to study the atmosphere at a 1-h interval.

The Keck AO data from July 30, 2007 consist of two parts. The initial observation has two consecutive 30-s intervals, though the first one has a corruption in its final 10-s segment. This gives us five 10-s measurements of the atmosphere. Then, 1 h later, we have 2.5 min of consecutive measurements, providing fifteen 10-s intervals.

Up to now we have dealt with the wind velocity vectors as measured by the WFS. This means that the velocities are all in millimeters per second as measured in the pupil. If the telescope is pointing away from zenith, this will cause the projection of the pupil onto the layer of frozen flow in the atmosphere to be elongated. This means that

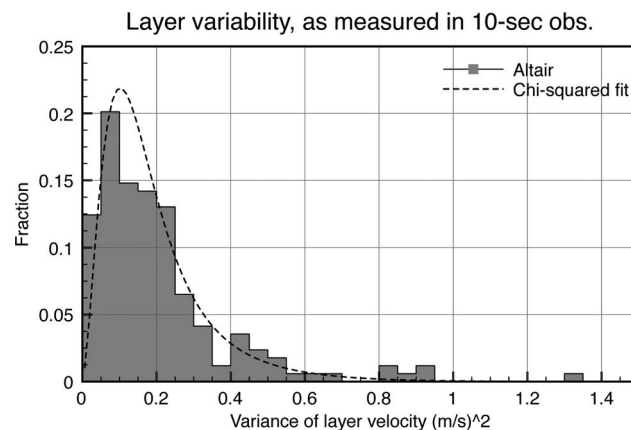


Fig. 8. Distribution of the sample variance of the velocity vectors for Altair at 10-s intervals. Well-fitted by a chi-squared distribution, the RMS motion is between 0.38 and 0.50 m/s.

the velocity estimates in the pupil are lower along one axis than the actual velocity on the sky. For the Altair data we have no pointing information and have hence ignored this effect. Furthermore, the Altair data were all taken during instrument setup, and so we can reasonably assume that the calibration was done on a star near zenith. This means that our layer velocity data (e.g., Fig. 7) is not significantly higher than what is occurring in the atmosphere.

The Keck data, in contrast, were taken during regular science observation, and the pointing information is known. This information allows us to deproject and rotate the pupil to produce the wind map on the sky. This is most useful when we have, as mentioned above, observations on the same night but at different times. Both July 30, 2007 observations were taken at similar zenith angles of near 45° . The observation 1 h later was at an azimuth 8°

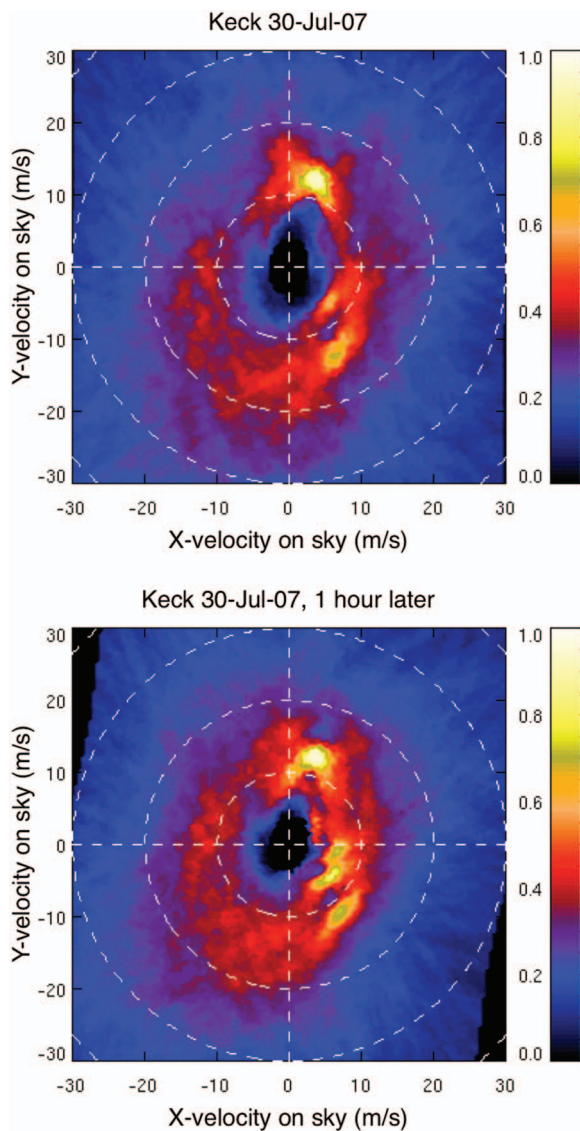


Fig. 9. Pointing/rotation adjusted wind maps showing likelihood (0 to 1) of a layer of frozen flow existing at a specific velocity vector, as measured by Keck AO 1 h apart. (Top) initial observation; (bottom) observation 1 h later, at different pointing. Note the strong similarity between the two wind maps, indicating that stability of layer velocities can exist on time scales of 1 h.

more than before. By projecting each velocity point in the wind map, we can transform the entire image to produce wind maps on the sky that can be directly compared.

Figure 9 shows transformed wind maps for the first 20-s period of the initial observation and the last 30-s period of the second observation 1 h later (1 h, 3 min, and 24 s later, to be exact). The similarity in the wind map structure is striking. Both observations have a very strong layer ($>95\%$ likelihood) at 12.5 m/s and 72° . In the first observation two more layers are found, one at 13.7 m/s and -61° , the other at 7.4 m/s and -37° . In the last observation there are now two layers at 11.8 m/s and -52° and 6.9 m/s and -30° .

We can examine the motion of this strong layer and the two more variable ones in detail for all five early and all fifteen late 10-s observations. Figure 10 plots the velocity vector locations, as determined by the watershed algorithm applied to the wind maps. In the left panel is the upper right quadrant of velocity space, with the strong layer. In the right panel, the lower right quadrant of velocity space is shown. For the 15 consecutive late measurements, the sample variances are estimated, as described above. The RMS layer variability, per axis, is estimated to be 0.054 m/s for the very strong and steady layer and 0.10 and 0.12 m/s for the two other layers.

We have two other Keck measurements that span several minutes. For the 18-Oct-07 data we follow two different 5-min measurements, one at 4 UT and one at 9 UT. In this case there was no similarity in the wind profile between these two measurements separated by 5 h. The 4-UT measurements observed one strong layer. Calculation of the sample variance produced an estimate of the RMS one-axis variability of the wind velocity of 0.051 m/s. In the 9-UT measurement, two strong layers were found. These had estimated RMS variation, per axis, of 0.18 and 0.47 m/s.

We have three different Keck observations of at least 2.5 min, which contained a total of six layers. Except for one case at 0.47 m/s, the layers had σ from 0.05 to 0.2 m/s, which is considerably below the variation estimated from Altair over 1-min intervals.

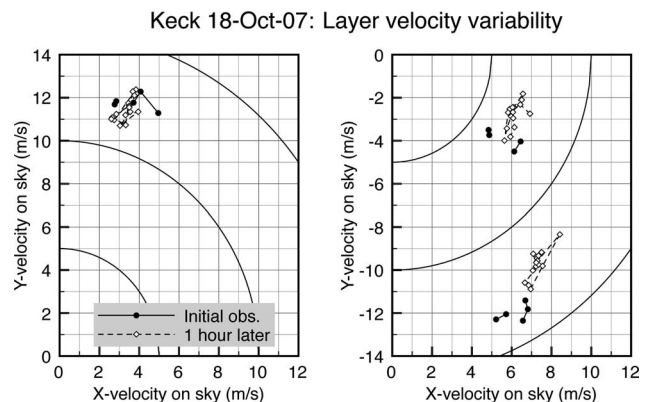


Fig. 10. Mapping of strongly detected layer wind velocities, for 10-s measurements, corresponding to the wind maps shown in Fig. 9. Solid data points, initial target; open data points, target 1 h later. All velocities adjusted for pointing/rotation. (Left panel) upper right quadrant, (right panel) lower right quadrant of velocity vector space.

C. Implications for Predictive Control

With the Altair data, we estimated that the inherent 10-s variability of the wind velocity vector (one-axis RMS) is in the range of 0.38 and 0.50 m/s; the Keck observations are mostly less than 0.20 m/s.

This level of inherent wind variability is reasonable for predictive control. For PFC, the strategy is to measure the wind and adapt the predictive control every 5 to 10 s. For predictive control to improve performance, it is necessary that the wind not change significantly in this short period between when the AO telemetry is recorded and the new control is used.

For PFC this translates directly into an examination of the temporal frequencies of the peaks of the temporal PSD of each Fourier mode. For each peak caused by a layer, the Kalman filter produces a notch in the error transfer function. If the wind velocity vector changes, the temporal frequency of the peak will change, following $f_t = (v_x + n_x)f_x + (v_y + n_y)f_y$, where the variables n_x and n_y represent the noise (variability) of the wind vector components. n_x and n_y being nonzero will cause f_t to change; if f_t moves by too much, it will no longer be centered in the notch of the Kalman filter and will not be predicted.

A change in f_t needs to be compared directly with the width of the notch in the error transfer function. For an AO system with $f_s = 1.5$ kHz, a moderate f_t (10 Hz or greater) in the Kalman filter provides at least 100 times more rejection of signal power than a regular integral controller at f_t . If the actual wind peak location is different from the filter's assumed f_t , the peak will start to move out of the notch, reducing this improvement. At $f_t \pm 4$ Hz, the predictor provides 10 times less rejection than at the bottom of the notch at f_t , but still at least 10 times more rejection than a regular integral controller.

An indirect way to assess this is to extrapolate the variance of f_t given the wind variability as estimated above. Assuming n_x and n_y are uncorrelated and both have variance σ^2 , the inherent RMS noise on the temporal frequency is $\sigma(f_x^2 + f_y^2)^{1/2}$. The maximum change in f_t occurs when $|f_x| = |f_y| = 1/(2d)$ (maximum controllable frequency). This maximum RMS noise on f_t is $\sigma/(d\sqrt{2})$. Based on the Altair and Keck data above, we make the conservative assumption that $\sigma = 0.5$ m/s. This means that for Altair's AO system, the maximum RMS motion a Fourier mode might see is 0.53 Hz. For Keck AO, the maximum is 0.63 Hz. For GPI, with its 18 cm subapertures, this amount would be 1.96 Hz, which is well within the $f_t \pm 4$ Hz range given above.

We can more directly assess the variability of f_t but only for the Keck and Altair data, not GPI, by examining the locations of the peaks that are found in the temporal PSDs. However, unlike the layer velocity vector case, we cannot make some simple assumptions. First, as indicated above, the amount of peak motion due to layer variability varies with spatial frequency of the mode examined. Second, our simulations indicate that even in the case of ideal frozen flow and low WFS noise, the PFC algorithms will have an inherent level of noise on the peak estimates. This noise is uncorrelated with spatial frequency and has only a weak correlation (about 0.3) with the magnitude of the temporal frequency of the peak. This prevents us from doing the same chi-squared fit as above,

since each spatial frequency will have a different inherent variance. Instead, we simply examine the distribution of the sample variances.

For the 117 nights of Altair data, we track roughly 22,000 unique peaks through the 1-min measurements. For each peak through time, we calculate the unbiased sample variance of the peak motion in Hz. This distribution is skewed more toward an exponential than a $\chi^2(N-1)$, but this is consistent with there being a range of inherent peak variation across the data points. For the Keck data we find the same type of distribution.

For the Altair data, 84% of the peaks had a sample variance under 1.0 Hz^2 and hence a RMS variation under 1.0 Hz. For the Keck data from 30-Jul-07 and 18-Oct-07, 79% of the peaks had a sample variance under 1.0 Hz^2 and hence a RMS variation under 1.0 Hz. However, in the Altair data only 38% of the peaks had an RMS variation under 0.53 Hz, and in the Keck data 51% of the peaks had an RMS variation under 0.63 Hz. This indicates that our formula above, which uses just the spatial frequency and the inherent wind variability, may not be sufficient to predict the peak motion in GPI.

D. Summary

If the velocity vector of a layer changes too rapidly, a predictive control algorithm will not be able to measure and adapt the control algorithm quickly enough to provide good performance. In our original proposal for PFC we baselined a 5–10 s update rate. Using the 117 nights of Altair data, we estimate that the inherent one-axis RMS variation of the velocity vector on 10-s intervals is between 0.38 and 0.50 m/s. From the Keck data, we find this RMS motion to be usually less than 0.20 m/s. Simulations indicate that this variability is due to the atmosphere, not to noise in the algorithms that are estimating the layer velocity vectors. This indicates that layers change velocity to only a small degree on 10-s time scales, indicating that PFC would be able to measure and adapt to the wind conditions on similar time scales, as proposed. In addition to this general characterization, we also provided a specific example from Keck AO where the wind profile had substantial stability in measurements taken 1 h apart.

Using a simple model that calculates peak variability from layer vector motion and spatial frequency, we estimate that GPI will see only about 2 Hz RMS peak motion, which is well constrained inside the notch. This will enable accurate prediction. Analysis of the actual peak motion indicates that Altair and Keck see less than 1 Hz RMS peak motion most of the time but that they see more motion than is predicted by our simple formula. If actual peak motion in GPI is significantly higher than the 2 Hz RMS that we estimate and exceeds the $f_t \pm 4$ criterion, this could be ameliorated by joint processing of the modes. Since the layer velocity vectors have low noise on the estimate (see above), an efficient version of the wind map algorithm could be developed and used in real time. After the peak finding, but before the Riccati solution for each mode, the layers would be determined and the peaks adjusted given the known layer profiles.

7. CONCLUSIONS

In this study we have applied the algorithms of PFC (and developed a few new ones) to analyze astronomical AO measurements of the turbulent atmosphere. Our goal was to see whether frozen flow could be easily detected and then, if so, determine whether PFC as formulated could be effective at predicting it. Frozen flow is easily detected at Mauna Kea at least 94% percent of the time. It contributed substantial power to the controllable phase (20%–40%), and contributes up to 70% for high-spatial-frequency modes. A high-order system like GPI, with spatial frequencies three times that of Keck AO, should see frozen flow with significant power and at temporal frequencies up to 100 Hz, which PFC is well suited to predict.

PFC must measure and adapt its control to prevailing atmospheric conditions for best performance. To do so it must accurately identify the layer velocities before they change. The one-axis RMS variation of the layer velocity vectors is estimated to be under 0.5 m/s on 10-s time scales, which implies that PFC could easily measure and adapt as currently proposed. This level of wind variability would cause the peaks to move away from the Kalman filter's specific f_i notch by 1.93 Hz for GPI, which would not significantly degrade performance. Direct measurements of Altair and Keck peak motion indicate that it is usually under 1 Hz RMS, though higher than we would predict due to layer variability alone.

This study is a very promising first step in turning the PFC proposal into an actual implementation. The next major step for us is to make an assessment of the performance advantage from using PFC under these observed atmospheric conditions, by estimating residual error. In the context of GPI, we would like to obtain similar AO telemetry sets from systems in Chile (preferably an AO system on Gemini South). Also, we are exploring how to conduct an on-sky test of PFC performance in an existing AO system. We are focusing on a time- and effort-efficient modification of a matrix-based real-time AO controller to implement the prediction. Offline, but rapid-response, telemetry analysis would update the predictive control laws.

ACKNOWLEDGMENTS

Lisa A. Poyneer thanks Mitch Troy for his initiative in acquiring the set of PALAO telemetry that got this project rolling. She also thanks Bruce Macintosh for his insightful commentary. We thank the Gemini Observatory staff for their work in obtaining Altair circular buffers for our analysis. The Gemini Observatory is operated by the Association of Universities for Research in Astronomy, Inc., under a cooperative agreement with the National Science Foundation on behalf of the Gemini partnership: the National Science Foundation (United States), the Science and Technology Facilities Council (United Kingdom), the National Research Council (Canada), CONICYT (Chile), the Australian Research Council (Australia), Ministério da Ciência e Tecnologia (Brazil), and SECYT (Argentina). Some of the data presented herein were obtained at the W. M. Keck Observatory, which is operated as a scientific

partnership among the California Institute of Technology, the University of California, and NASA. The Observatory was made possible by the generous financial support of the W. M. Keck Foundation. The authors wish to recognize and acknowledge the very significant cultural role and reverence that the summit of Mauna Kea has always had within the indigenous Hawaiian community. We are most fortunate to have the opportunity to conduct observations from this mountain.

This work was performed under the auspices of the U.S. Department of Energy by Lawrence Livermore National Laboratory under contract DE-AC52-07NA27344. The document number is LLNL-JRNL-407053. This work has been supported by the National Science Foundation (NSF) Science and Technology Center for Adaptive Optics, managed by the University of California at Santa Cruz under cooperative agreement AST-9876783.

REFERENCES

1. B. Macintosh, J. Graham, D. Palmer, R. Doyon, D. Gavel, J. Larkin, B. Oppenheimer, L. Saddlemyer, J. K. Wallace, B. Bauman, J. Evans, D. Erikson, K. Morzinski, D. Phillion, L. Poyneer, A. Sivaramakrishnan, R. Soummer, S. Thibault, and J.-P. Véran, "The Gemini Planet Imager," *Proc. SPIE* **6272**, 62720L (2006).
2. T. Fusco, C. Petit, G. Rousset, J.-F. Sauvage, K. Dohlen, D. Mouillet, J. Charton, P. Baudoz, M. Kasper, E. Fedrigo, P. Rabou, P. Feautrier, M. Downing, P. Gigan, J.-M. Conan, J.-L. Beuzit, N. Hubin, F. Wildi, and P. Puget, "Design of the extreme AO system for SPHERE, the planet finder instrument of the VLT," *Proc. SPIE* **6272**, 62720K (2006).
3. D. T. Gavel and D. Wiberg, "Towards Strehl-optimizing adaptive optics controllers," *Proc. SPIE* **4839**, 890–901 (2002).
4. B. Le Roux, J.-M. Conan, C. Kulcsar, H.-F. Raynaud, L. M. Mugnier, and T. Fusco, "Optimal control law for classical and multiconjugate adaptive optics," *J. Opt. Soc. Am. A* **21**, 1261–1276 (2004).
5. K. Hinnen, M. Verhagen, and N. Doelman, "Exploiting the spatiotemporal correlation in adaptive optics using data-driven \mathcal{H}_2 -optimal control," *J. Opt. Soc. Am. A* **24**, 1714–1725 (2007).
6. L. A. Poyneer, B. A. Macintosh, and J.-P. Véran, "Fourier transform wavefront control with adaptive prediction of the atmosphere," *J. Opt. Soc. Am. A* **24**, 2645–2660 (2007).
7. O. Guyon, "Limits of adaptive optics for high-contrast imaging," *Astrophys. J.* **629**, 592–614 (2005). Revised version at <http://arxiv.org/abs/astro-ph/0505086>.
8. M. C. Britton, "Arroyo," *Proc. SPIE* **5497**, 290–300 (2004).
9. E. Gendron and P. Lena, "Single layer atmospheric turbulence demonstrated by adaptive optics observations," *Astrophys. Space Sci.* **239**, 221–228 (1996).
10. M. Schöck and E. J. Spillar, "Method for a quantitative investigation of the frozen flow hypothesis," *J. Opt. Soc. Am. A* **17**, 1650–1658 (2000).
11. J. A. Stoesz, J.-P. Véran, F. J. Rigaut, G. Herriot, L. Jolissaint, D. Frenette, J. Dunn, and M. Smith, "Evaluation of the on-sky performance of altair," *Proc. SPIE* **5490**, 67–78 (2004).
12. M. A. van Dam, D. L. Mignant, and B. A. Macintosh, "Performance of the Keck Observatory adaptive-optics system," *Appl. Opt.* **43**, 5458–5467 (2004).
13. L. A. Poyneer and B. Macintosh, "Spatially filtered wavefront sensor for high-order adaptive optics," *J. Opt. Soc. Am. A* **21**, 810–819 (2004).
14. L. A. Poyneer, D. T. Gavel, and J. M. Brase, "Fast wavefront reconstruction in large adaptive optics systems with use of the Fourier transform," *J. Opt. Soc. Am. A* **19**, 2100–2111 (2002).
15. L. A. Poyneer and J.-P. Véran, "Optimal modal Fourier

- transform wave-front control,” J. Opt. Soc. Am. A **22**, 1515–1526 (2005).
16. M. Frigo and S. G. Johnson, “The design and implementation of FFTW3,” Proc. IEEE **93**, 216–231 (2005). (Special issue: “Program Generation, Optimization, and Platform Adaptation.”)
 17. A. V. Oppenheim, R. W. Schaffer, and J. R. Buck, *Discrete-Time Signal Processing* (Prentice Hall, 1999).
 18. L. A. Poyneer and D. Dillon, “MEMS adaptive optics for the Gemini Planet Imager: control methods and validation,” Proc. SPIE **6888**, 68880H (2008).
 19. F. Roddier, *Adaptive Optics in Astronomy* (Cambridge U. Press, 1999).
 20. C. Petit, J. M. Conan, C. Kulcsár, H. F. Raynaud, and T. Fusco, “First laboratory validation of vibration filtering with LQG control law for adaptive optics,” Opt. Express **16**, 87–97 (2008).
 21. R. C. Gonzalez and R. E. Woods, *Digital Image Processing* (Prentice Hall, 2002).
 22. L. A. Poyneer and B. A. Macintosh, “Optimal Fourier control performance and speckle behavior in high-contrast imaging with adaptive optics,” Opt. Express **14**, 7499–7514 (2006).
 23. E. M. Johansson and D. T. Gavel, “Simulation of stellar speckle imaging,” Proc. SPIE **1237**, 372–383 (1994).
 24. A. Papoulis and S. U. Pillai, *Probability, Random Variables and Stochastic Processes*, 4th ed. (McGraw Hill, 2002).